# Nanoparticle-Tuned Self-Organization of a Bulk Heterojunction Hybrid Solar Cell with Enhanced Performance

13 AUTHORS, INCLUDING:

Cheng-Si Tsao
Institute of Nuclear Energy Research
40 PUBLICATIONS   689 CITATIONS

SEE PROFILE

chih-min Chuang
Institute of Nuclear Energy Research
27 PUBLICATIONS   361 CITATIONS

SEE PROFILE

Yu-Ching Huang
Institute of Nuclear Energy Research
34 PUBLICATIONS   421 CITATIONS

SEE PROFILE

Yang-Fang Chen
National Taiwan University
502 PUBLICATIONS   7,706 CITATIONS

SEE PROFILE

# Nanoparticle-Tuned Self-Organization of a Bulk Heterojunction Hybrid Solar Cell with Enhanced Performance

Hsueh-Chung Liao,[†] Cheng-Si Tsao,[‡,*] Tsung-Han Lin,[†] Meng-Huan Jao,[†] Chih-Min Chuang,[‡] Sheng-Yong Chang,[§] Yu-Ching Huang,[‡] Yu-Tsun Shao,[§] Charn-Ying Chen,[‡] Chun-Jen Su,[⊥] U-Ser Jeng,[⊥] Yang-Fang Chen,[§] and Wei-Fang Su[†,*]

[†]Department of Materials Science and Engineering, National Taiwan University, Taipei 106-17, Taiwan, [‡]Institute of Nuclear Energy Research, Longtan, Taoyuan 325-46, Taiwan, [§]Department of Physics, National Taiwan University, Taipei 106-17, Taiwan, and [⊥]National Synchrotron Radiation Research Center, Hsinchu 300-77, Taiwan.

**B**ulk heterojunction (BHJ) polymer solar cells show great promise for providing low-cost, lightweight, large-area, and mechanically flexible energy conversion devices. BHJ polymer blends that consist of poly(3-hexylthiophene) and [6,6]-phenyl-C61-butyric acid methyl ester (P3HT/PCBM) have shown promising power conversion efficiency (PCE).[1−4] The device performance of the P3HT/PCBM polymer solar cells critically depends on the three-dimensional self-organized nanostructure of the active layer.[5−10] This nanostructure is formed by separation of the nanodomains of P3HT and PCBM-related phases in BHJ thin films. Such phase separation constructs an interpenetrating or bicontinuous network with effective charge separation and carrier transport. Control over the nanostructure (film morphology) is classically attained by thermal or solvent annealing processes.[1−3,7−15] The challenge of optimizing the annealing process has been largely resolved. Recently though, manipulation of phase-separated nano-structures by stepwise annealing treatments was reported.[7] Use of inorganic/organic hybrid solar cells is a potential approach for improving device performance. An effective architecture for highly efficient hybrid polymer solar cells was obtained by placing an ordered nanorod (or porous) template adjacent to the P3HT/PCBM layer, significantly increasing the paths of carrier collection and transport.[16−19] Unfortunately, this complicated process is impractical for large-area solar cell fabrication such as roll-to-roll process. Previous studies of hybrid solar cells have directly incorporated inorganic nanoparticles (INPs) as electron acceptors (ZnO, TiO$_x$, or CdSe INPs),[20−23] light-harvesting absorbers, or light-scattering centers (Au, Ag, or CdSe INPs)[24−28] in conjugated polymer film.

## ABSTRACT
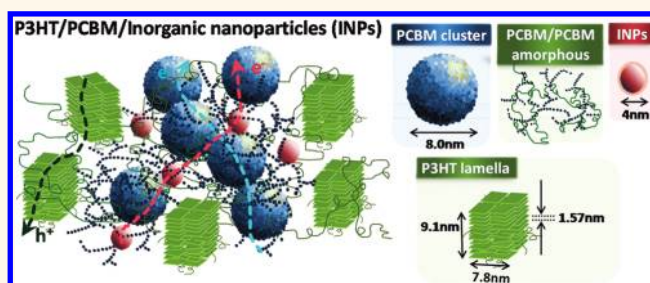


We demonstrate here that the nanostructure of poly(3-hexylthiophene) and [6,6]-phenyl-C61-butyric acid methyl ester (P3HT/PCBM) bulk heterojunction (BHJ) can be tuned by inorganic nanoparticles (INPs) for enhanced solar cell performance. The self-organized nanostructural evolution of P3HT/PCBM/INPs thin films was investigated by using simultaneous grazing-incidence small-angle X-ray scattering (GISAXS) and grazing-incidence wide-angle X-ray scattering (GIWAXS) technique. Including INPs into P3HT/PCBM leads to (1) diffusion of PCBM molecules into aggregated PCBM clusters and (2) formation of interpenetrating networks that contain INPs which interact with amorphous P3HT polymer chains that are intercalated with PCBM molecules. Both of the nanostructures provide efficient pathways for free electron transport. The distinctive INP-tuned nanostructures are thermally stable and exhibit significantly enhanced electron mobility, external quantum efficiency, and photovoltaic device performance. These gains over conventional P3HT/PCBM directly result from newly demonstrated nanostructure. This work provides an attractive strategy for manipulating the phase-separated BHJ layers and also increases insight into nanostructural evolution when INPs are incorporated into BHJs.

However, to the best of our knowledge, there is no report using INPs as a strategy to effectively control the nanostructure of the P3HT/PCBM active layer. Furthermore, few studies have focused on the fundamental details of nano-structural variation as influenced by the direct addition of INPs.

This is the first demonstration that the nanostructure of a P3HT/PCBM BHJ film can be tuned by INP incorporation. Our process

is substantially different from the phase separations controlled merely by solvent or thermal annealing treatments.[1−3,7−15] This phase-separated nanostructure can be attained by incorporating a specific amount of INPs without thermal annealing and/or solvent annealing. Herein, we refer to the self-organized nanostructure that is tuned by the interaction of incorporated INPs with the other components during phase separation as "nanoparticle-tuned nanostructure". In this study, we have fabricated two types of solar cells composed of these new nanoparticle-tuned nanostructures. For comparison, the devices were made with annealing or without to illustrate the significant improvements in PCE and external quantum efficiency (EQE). From a fundamental viewpoint, the nanoparticle-tuned self-organized nanostructure provides some insight into principles for manipulating phase separation in the P3HT/PCBM films and, also, thus providing a novel approach for effectively varying the self-organized nanostructure (or 3D morphology) of BHJ films. Our new tuning method is a simple and annealing-free treatment that allows for fabrication of large-area solar cells including those made by the roll-to-roll process.

We have systematically investigated the effect of varying amounts of $Cu_2S$ INPs upon the formation of nanoparticle-tuned nanostructure. The detailed nanostructures of the spatially aggregated PCBM phase and organization of P3HT-related phases in the P3HT/PCBM/$Cu_2S$ INP hybrid film were quantitatively characterized by using simultaneous grazing-incidence small-angle X-ray scattering (GISAXS) and wide-angle X-ray scattering (GIWAXS) techniques. Notably, we found that devices treated with an additional thermal annealing were also positively affected by the inclusion of INPs. The morphological results can be correlated with device performance. We found that significant PCE improvements of 55% (from 1.1 to 1.7%) for the as-casted sample and 23% (from 3.5 to 4.3%) for the thermal annealed sample were obtained due to the formation of nanoparticle-tuned nanostructures facilitating effective carriers' separation and transportation. In the case where cadmium selenide (CdSe) is the incorporated INP in the P3HT/PCBM BHJ film, similar improvement was seen. This result underscores that different kinds of INPs have potential for tuning the phase-separated nanostructure of P3HT/PCBM BHJ. The new findings of this study of INP-tuned P3HT/PCBM nanostructures advance the fundamental study and technological application of the familiar P3HT/PCBM BHJ polymer solar cell.

## RESULTS AND DISCUSSION

The INPs used in this study ($Cu_2S$ and CdSe) were 4−5 nm in diameter, and the transmission electron microscope (TEM) images of the synthesized INPs are shown in the Supporting Information, Figure S1. The correlation of structural characterization and device performance is discussed with respect to pristine polymer P3HT film, P3HT/PCBM blended film, and P3HT/PCBM/$Cu_2S$ INPs hybrid films containing three different concentrations of $Cu_2S$ INPs, respectively, that is, low concentration, $1.2 \times 10^{-2}$ vol %; medium concentration, $6.2 \times 10^{-2}$ vol %; and high concentration, $6.2 \times 10^{-1}$ vol % (see Experimental Method for detailed sample preparation). These film samples are denoted as PO, BL, HY_L, HY_M, and HY_H. In this case, the simultaneous GISAXS/GIWAXS characterization of the films reveals that distinctive phase-separated nanostructures can be tuned by incorporating a critical volume fraction of $Cu_2S$ INPs, $6.2 \times 10^{-2}$ vol %. This remarkable structure of the HY_M sample and the other hybrid samples was further treated by thermal annealing to form different nanostructures (denoted as BL_A, HY_L_A, HY_M_A, and HY_H_A). The morphology was characterized by the GISAXS/GIWAXS. The individual evolution behavior is governed by the original structure formed at the as-casted state. Subsequently, nanoparticle-tuned device performance (with and without the thermal treatment) significantly improves due to the effect of INPs upon nanostructural characteristics. We also tested the photovoltaic property of P3HT/PCBM/$Cu_2S$ hybrid films with largely increased amounts of INPs (>$6.2 \times 10^{-1}$ vol %). The instrumental setup and measurement procedure of this simultaneous GISAXS/GIWAXS technique are described elsewhere.[8] In this study, the GIWAXS profiles are a function of scattering vector $Q$ and are reduced from the corresponding 2D GIWAXS patterns along the out-of-plane direction (i.e., perpendicular to the substrate and film surface; defined as $Q_Z$ direction). The GISAXS profiles were reduced from the corresponding GISAXS patterns along the in-plane direction (i.e., parallel to the substrate; defined as $Q_X$ direction). The in-plane GISAXS profiles are mainly used to determine the structures of the PCBM clusters and INPs. Furthermore, the out-of-plane GIWAXS profiles reveal the lamellar spacing and crystallinity of edge-on P3HT crystalline domain with lamellar layers. In short, the crystalline domains with lamellar layers oriented in parallel and perpendicular to the substrate are defined as edge-on and face-on, respectively. The edge-on domains in the P3HT/PCBM film are the representative P3HT crystallites as compared to the face-on domains.[7,8,29,30] Regarding the crystallographic directions of the polymer molecules of the edge-on domain, the lamellar layers lie in the (100) plane. The direction of hexyl side chains, [100], is normal to the layers with the thiophene rings that lie in (010) plane. Hence, the $\pi-\pi$ stacking direction is normal to the (010) plane. As a result, in the 2D GIWAXS patterns, the (100), (200), and (300) peaks would appear in the out-of-plane

direction along $Q_X = 0$ Å$^{-1}$, while the (010) peak would appear in the in-plane direction along $Q_Z = 0.38$ Å$^{-1}$.[7] Also, the (100) peak of the face-on domain with the $\pi$ face parallel to the substrate would appear in the in-plane direction along $Q_Z = 0$ Å$^{-1}$ (see 2D GIWAXS patterns in Supporting Information, Figure S2).

**Simultaneous GISAXS/GIWAXS characterization for as-casted films.** The GIWAXS and GISAXS profiles for the pristine P3HT, P3HT/PCBM blending film, and P3HT/PCBM/Cu$_2$S hybrid films are shown in Figure 1a,b, respectively (the corresponding 2D patterns are shown in the Supporting Information, Figure S2). The calculated lamellar spacing ($=2\pi/Q_Z$) as indicated by the position of (100) peaks in Figure 1a is summarized in Table 1. We observe that the lamellar spacing of the blended film (16.6 Å) is larger than that of the pristine P3HT film (15.8 Å), as evidenced by the shift of (100) peak toward the low-Q region[31] (Figure 1a and Table 1). The literature[31,32] pointed out that the expansion effect is due to the intercalation of PCBM molecules between lamellar layers. Of note, the lamellar spacing of the edge-on P3HT crystalline domain in the nanoparticle-tuned nanostructure (HY_M film, 15.7 Å) is almost the same as that in the pristine P3HT film (15.8 Å). On the other hand, the lamellar spacing of the P3HT/PCBM/Cu$_2$S INP hybrid films (HY_L and HY_H films, 16.4 Å) are close to that of the P3HT/PCBM blended film (BL film) with a lamellar spacing of 16.6 Å. Since these results correspond to hybrid films with either the lowest and highest amount of Cu$_2$S, we conclude that such amount of INPs has no effect on the lamellar spacing of P3HT crystallites. Important though, the hybrid film with a medium amount of Cu$_2$S (*i.e.*, nanoparticle-tuned nanostructure) exhibits characteristics similar to the pristine P3HT, where it seems no PCBM molecule intercalated in the P3HT crystalline domains. This behavior should be closely related to the formation of PCBM aggregation into cluster domains that mutually compete and interact with the crystallization of P3HT during the phase separation process (further discussion below). Moreover, a previous study[8] demonstrated that the presence of PCBM molecules attenuates the nucleation rate (or crystallization degree) of P3HT crystal in the P3HT/PCBM composite. Therefore, the relatively low (100) peak intensity in the nanoparticle-tuned nanostructure suggests that its crystallization is significantly limited or affected by the PCBM molecules dispersed in the hybrid solution.

Our previous study[33] showed that P3HT-rich domains are categorized into two types: (1) the PCBM molecules intercalated in P3HT crystalline domain[31,32] (so termed the P3HT-crystal/PCBM domain and characterized by GIWAXS) and (2) the network structure of PCBM molecules intercalated within the amorphous P3HT phase (so termed PCBM/P3HT amorphous domain and detectable by GISAXS). The GISAXS profile in the low-Q region (<0.01 Å$^{-1}$) has an upturn with
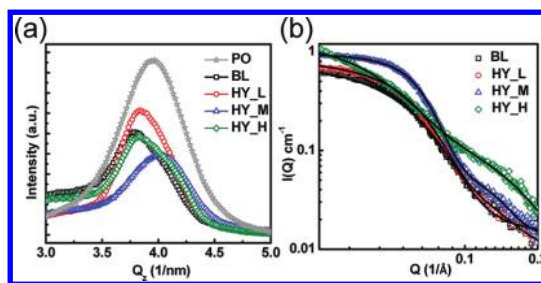


**Figure 1.** (a) Out-of-plane GIWAXS and (b) in-plane GISAXS profiles along the $Q_Z$ and $Q_X$ directions, respectively, for the as-casted pristine P3HT film (PO), P3HT/PCBM blended film (BL), and P3HT/PCBM/Cu$_2$S INPs hybrid films (HY_L, HY_M, and HY_H). The solid lines represent the fitted GISAXS intensities.

**TABLE 1. Structural Parameters Obtained by Model Fitting and the Corresponding Photovoltaic Characteristics and Electron Mobility of As-Casted Pristine Polymer (PO), P3HT/PCBM Blended Film (BL), P3HT/PCBM/Cu$_2$S INP Hybrid Films (HY_L, HY_M, and HY_H), Annealed P3HT/PCBM Blended Film (BL_A), and P3HT/PCBM/Cu$_2$S INP Hybrid Films (HY_L_A, HY_M_A, and HY_H_A)**

| BHJ films | lamellar spacing (Å) | $\eta_P$ (%) | $R$ (nm) | $V_{oc}$ (V) | $J_{sc}$ (mA/cm$^2$) | FF (%) | PCE (%) | $\mu_e$ (cm$^2$/(V·s)) |
|---|---|---|---|---|---|---|---|---|
| P0 | 15.8 | | | | | | | |
| BL | 16.6 | 6.1 | 2.8 | 0.64 | 4.7 | 37 | 1.1 | $2.2 \times 10^{-7}$ |
| HY_L | 16.4 | 6.5 | 3.3 | 0.59 | 6.3 | 35 | 1.3 | $6.4 \times 10^{-7}$ |
| HY_M | 15.7 | 11.8 | 3.9 | 0.60 | 7.5 | 38 | 1.7 | $1.0 \times 10^{-6}$ |
| HY_H | 16.4 | 5.4 | 3.2 | 0.57 | 6.1 | 37 | 1.3 | $4.8 \times 10^{-7}$ |
| BL_A | 15.9 | 20.0 | 4.9 | 0.59 | 10.1 | 59 | 3.5 | $1.6 \times 10^{-5}$ |
| HY_L_A | 16.4 | 13.2 | 5.0 | 0.59 | 10.5 | 60 | 3.7 | $1.0 \times 10^{-4}$ |
| HY_M_A | 16.5 | 11.9 | 5.2 | 0.59 | 11.8 | 61 | 4.3 | $1.3 \times 10^{-4}$ |
| HY_H_A | 16.6 | 9.3 | 4.8 | 0.54 | 11.4 | 60 | 3.8 | $6.7 \times 10^{-5}$ |

respect to power-law behavior (Supporting Information, Figure S3). This upturn directly results from the PCBM/P3HT amorphous domain,[7] which is not included in the present quantitative analysis. The behavioral results were fitted to include the low-Q upturn using the model from our previous study. We see that such inclusion does not influence the results that are fitted using the below model (Supporting Information, Figure S4).

During phase separation, PCBM clusters (nanodomain) are usually formed by aggregation and diffusion of PCBM molecules out of the P3HT-rich polymer regions. The GISAXS profiles in the medium- and high-Q region (>0.03 Å$^{-1}$), as shown in Figure 1b, result from the PCBM clusters and Cu$_2$S INPs. The PCBM clusters dominate the GISAXS intensity because of their larger size (6−18 nm) and higher volume as compared to the Cu$_2$S INPs (~4 nm in size). The GISAXS intensity profile that is contributed by the PCBM clusters can be expressed as follows[7,8,34]

$$I_{PCBM}(Q) = \eta_P V_P (\Delta\rho_P)^2 \left[ \int_0^\infty F_i^2(Q, \sigma_i) f(\sigma_i) d\sigma_i \right.$$

$$\left. + \int_0^\infty \int_0^\infty F_i(Q, \sigma_i) F_j(Q, \sigma_j) H_{ij}(Q, \sigma_i, \sigma_j) f_i(\sigma_i) f_j(\sigma_j) d\sigma_i d\sigma_j \right]$$

$$(1)$$

$$F_i(Q, \sigma_i) = 4\pi \left[ \sin(Q\sigma_i/2) - \frac{1}{2}Q\sigma_i\cos(Q\sigma_i/2) \right] \quad (2)$$

where $\eta_P$ is the volume fraction of the PCBM cluster, $\Delta\rho_P$ is the difference in scattering length density (SLD) between the PCBM cluster and the surrounding matrix. Here, it is assumed that PCBM clusters are polydispersed spheres having Schultz size distribution with hard-sphere interaction between clusters.[35] $V_P$ is the average cluster volume. $F_i(Q,\sigma_i)^2$ is the form factor of a spherical cluster with a diameter $\sigma_i$. $H(Q,\sigma_i,\sigma_j)$ is the pair structure function that describes the interaction between clusters with Percus–Yevick approximation. $R_0$ is the mean cluster radius. The polydispersity, $p$, is defined as $a/R_0$, where $a^2$ of is the variance of Schultz size distribution $f(\sigma)$. The GISAXS profile contributed by both PCBM clusters and polydispersed spherical $Cu_2S$ INPs can be given by

$$I(Q) = I_{PCBM}(Q) + c \int_0^\infty R^6 g(R) F^2(Q, R) dR \quad (3)$$

where the constant $c$ is related to the product of volume fraction and scattering contrast of the $Cu_2S$ INPs having Schultz size distribution $g(R)$. All profiles can be well-fitted using eq 3, as shown by the solid curves in Figure 1b. The structural parameters of the PCBM clusters and $Cu_2S$ INPs are determined from the model, fitted according to eq 3 for the blended films, and hybrid films are summarized in Table 1. Essentially, the polydispersed hard-sphere model describes that the cluster size and spatial distribution of PCBM domains dominates the GISAXS intensity. The contribution by spherical $Cu_2S$ INPs is mainly in the high-$Q$ region. Figure 2 is an example of this where the GISAXS intensity for the HY_M film fitted using a nonlinear least-squares technique[36] over the entire $Q$ region (0.03–0.2 $Å^{-1}$) can be resolved into two GISAXS intensity profiles by calculating the polydispersed spheres' form factor ($Cu_2S$ INPs) and polydispersed hard-sphere model (PCBM clusters), respectively. The mean cluster radius and volume fraction ($R = 2.8$ nm; $\eta = 6.1\%$) of PCBM in the as-casted P3HT/PCBM blended film (BL) was determined by the model fitting and marginally agree with those of our previous study[7] and others.[8,34] The difference between the reported results is due to the different processing and material batches.

Looking at the hybrid films with low and high amounts of $Cu_2S$ INPs reveals that the inclusion of $Cu_2S$ INPs has no significant effect on the volume fraction of PCBM clusters formed during the phase separation as compared to that of the blended film. Interestingly, the nanoparticle-tuned nanostructure displays a much higher fraction of PCBM clusters (11.8%; ~2 times that of P3HT/PCBM blended film, BL) due to the presence of a critical amount (6.2 × $10^{-2}$ vol %) of $Cu_2S$ INPs. This remarkable phenomenon on nanoparticle-assisted aggregation is reported for the first time. Additionally, the hybrid films generally have
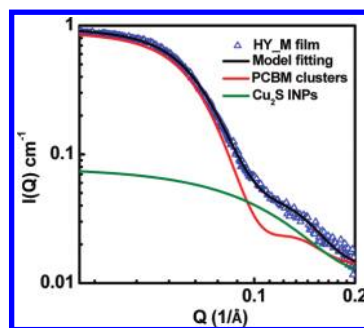


**Figure 2.** Fitted GISAXS intensity of the HY_M film, resolved into two GISAXS intensity profiles contributed by the $Cu_2S$

**TABLE 2. Photovoltaic Device Characteristics of P3HT/PCBM Blend and P3HT/PCBM/$Cu_2S$ INP Hybrid Films with Largely Increased Amount of Incorporated INPs**

| concentration (vol %) | $V_{oc}$ (V) | $J_{sc}$ (mA/cm²) | FF (%) | PCE (%) |
|---|---|---|---|---|
| P3HT/PCBM | 0.59 | 10.1 | 60 | 3.5 |
| 6.2 × $10^{-1}$ (HY_H_A) | 0.54 | 11.4 | 60 | 3.8 |
| 2.4 | 0.48 | 8.0 | 48 | 1.88 |
| 5.8 | 0.38 | 4.0 | 36 | 0.56 |
| 11.0 | 0.37 | 3.3 | 37 | 0.45 |

INPs and PCBM clusters, respectively.

slightly larger sized PCBM clusters ($R = 3.3$ and $3.2$ nm for HY_L and HY_H, respectively) than that of the blended film ($R = 2.8$ nm) without dependence upon the amount of incorporated $Cu_2S$ INPs. Notably, the nanoparticle-tuned nanostructure (HY_M film) has the largest cluster size ($R = 3.9$ nm) among the hybrid films. Therefore, incorporating the INPs has a potential effect on the growth of aggregated PCBM clusters.

**Correlation of Nanostructure to Device Performance and Electron Mobility.** We further investigated the characteristics of the nanoparticle-tuned nanostructure, by correlating the nanostructure of both blended and hybrid films to device performance and electron mobility (listed in Table 2). The photocurrent–voltage curves and the electron mobility measurements are shown in the Supporting Information, Figure S5. The electron mobilities of hybrid film with low and high amounts of $Cu_2S$ (HY_L = 6.4 × $10^{-7}$ cm²/(V·s) and HY_H = 4.8 × $10^{-7}$ cm²/(V·s)) are slightly higher than that of blended film (BL = 2.2 × $10^{-7}$ cm²/(V·s)). This results from the larger cluster size of PCBM and enhanced interpenetrating network (pathways for carrier transport) due to the presence of INPs. Their corresponding short-circuit current densities consistently outperform that of blended film. Notably, the electron mobility of the HY_M film is significantly improved up to 1.0 × $10^{-6}$ cm²/(V·s) directly due to the nanoparticle-tuned nanostructure (larger volume fraction and radius of PCBM clusters). The short-circuit current densities and PCE of HY_M hybrid solar cell are enhanced to 7.5 mA/cm² and 1.7% compared to those of BL blended solar cell (4.7 mA/cm² and 1.1%), again directly due to the

presence of distinctive nanostructure. This reveals that an effective network for charge carrier transportation exists in the nanoparticle-tuned nanostructure. The relatively low fill factor and low electron mobility as compared to the previously reported values are noteworthy. We attribute this to poor contact between the active layer and the cathode Al which typically can be improved by a postproduct thermal annealing process (*i.e.*, annealing the device with cathode Al on the top).[1,2,7] Therefore, the overall PCE of the corresponding solar cell remains low without thermal annealing, but the systematic trend of PCE can serve as a relative index for device performance. Thus, the nanoparticle-tuned nanostructure formed by the spin-coating processes can significantly enhance the performance and electron mobility.

**Formation of Nanoparticle-Tuned Nanostructure.** The GISAXS/GIWAXS characterization demonstrates that the nanoparticle-assisted aggregation of PCBM clusters is concomitant with the disappearance of PCBM molecules intercalated in the P3HT crystallites. This raises an interesting issue: How is the nanostructure significantly tuned by a certain amount of $Cu_2S$ INPs? According to the results of our systematic characterization, we propose a phenomenological mechanism for formation of this distinctive structure. If the amount of incorporated $Cu_2S$ NPs is very low (like HY_L film), the phase separation or structure of BHJ blended film is almost not affected by the addition of INPs. If the amount of $Cu_2S$ INPs is relatively high (like HY_H film), the $Cu_2S$ INPs will naturally form aggregate-like structure (nanodomains) as an impurity phase, and thus the remaining INPs dispersed in the film are made very dilute. When the amount of $Cu_2S$ INPs is appropriately in the medium, the INPs would uniformly disperse in the blended solution (before phase separation). This spatial effect amplifies the distinctive interaction between INPs, PCBM molecules, and P3HT molecules *in situ*. Due to the surface functional groups and the steric hindrance of INPs in the solution, the intercalation[31,32] among the polymer chains, PCBM molecules, and INPs occurs. In this situation, the INPs can be regarded as nuclei to intercalate (or block) polymer chains and PCBM molecules that facilitate the formation of a zone with a high density of PCBM molecules surrounding the nuclei. Additionally, the uniformly dispersed zones connect with one another to form a structural network within the polymer solution. This network can be regarded as a remarkable phase with abundant PCBM molecules (termed here as PCBM-dense zone and illustrated in Figure 3). This phase leads to several zones of very dilute PCBM molecules in the other local regions (herein termed PCBM-diluted zone).

It follows that phase separation begins during spin-coating process; the P3HT crystallite without PCBM molecules inside would form in the PCBM-diluted zones, as evidenced by the GIWAXS pattern with the same peak position as that of the pristine P3HT film, but with a low peak intensity (low crystallinity). Meanwhile, the PCBM concentration of some local regions in the PCBM-dense zones is supersaturated, which is the typical driving force for nucleation and growth of cluster domains. This explains why the GISAXS detects a high volume fraction and large size of PCBM clusters in the nanoparticle-tuned nanostructure. For the regular BL blended film, the driving force necessary to form PCBM clusters is the supersaturation of PCBM concentration that comes from evaporation of the solvent. The spatial arrangement of PCBM clusters, P3HT-crystal/PCBM domain,[31−33] and the PCBM/P3HT amorphous domain[7] in the BHJ film is illustrated in Figure 4a. For the HY_M hybrid film, the PCBM-dense phase arises from the INPs; INPs are an additional driving force that allow for higher fraction and larger sizes of PCBM clusters in the BHJ structure (Figure 4b). Therefore, the resultant interconnecting PCBM clusters provide a better, more continuous pathway for charge carrier transport over typical blended films (represented in Figure 4b as a light blue transporting route). Moreover, the uniform dispersion of $Cu_2S$ INPs can interact with the amorphous P3HT polymer chains intercalated with PCBM molecules (*i.e.*, PCBM/P3HT amorphous domain). This provides yet another transport pathway. This may then couple with the original pathway consisting of PCBM clusters (Figure 4b, red transporting route) and their spatial distribution to effectively enhance the effect of charge transport. Both of the constructed transport pathways are tuned by INPs leading to enhanced electron mobility and device performance (Table 1).

**Variation of Nanoparticle-Tuned Nanostructure with Thermal Annealing.** The GIWAXS and GISAXS profiles for the films with additional thermal annealing (*i.e.*, BL_A, HY_L_A, HY_M_A, and HY_H_A films) are shown in Figure 5a,b, respectively. The corresponding 2D patterns are shown in the Supporting Information, Figure S6. The GIWAXS profile for the nanoparticle-tuned nanostructure (HY_M_A film) reveals an unusual shift in peak position when compared to films without additional thermal annealing. The lamellar spacing of the new structure after thermal annealing is comparable to that of the regular blended or hybrid films with PCBM molecules intercalated in P3HT crystallites (Table 1). Our explanation for the variation of lamellar spacing is as follows: when the sample was thermally treated, a large amount of the P3HT crystallites begin to form in the PCBM-dense zones,[29] creating a P3HT crystallite with intercalated PCBM molecules. Some of the originally small P3HT crystallites may be soluble during the annealing process.[8] For the other blended and hybrid films treated with additional annealing, the (100) peak position of their GIWAXS profiles is relatively unchanged. Note that the GIWAXS profiles of the annealed films with incorporated INPs have a pronounced shoulder. The shoulder may arise from an overlap with a minor peak due to the slight variation in the lamellar spacing. Therefore, INPs have little effect upon the crystallization of P3HT during thermal annealing.

The GISAXS profiles of Figure 5b can be well-fitted using the model mentioned previously (solid lines).
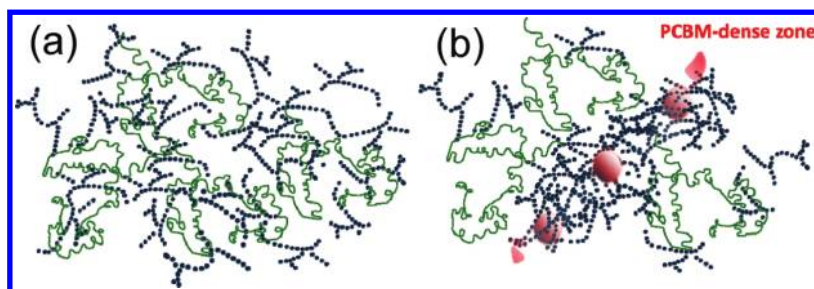
**Figure 3.** Schematic representation of (a) amorphous polymer chains intercalated with PCBM molecules in the regular P3HT/PCBM blended solution and (b) dispersed INPs as nuclei (in the polymer solution) to intercalate polymer chains and PCBM molecules to form PCBM-dense zone.
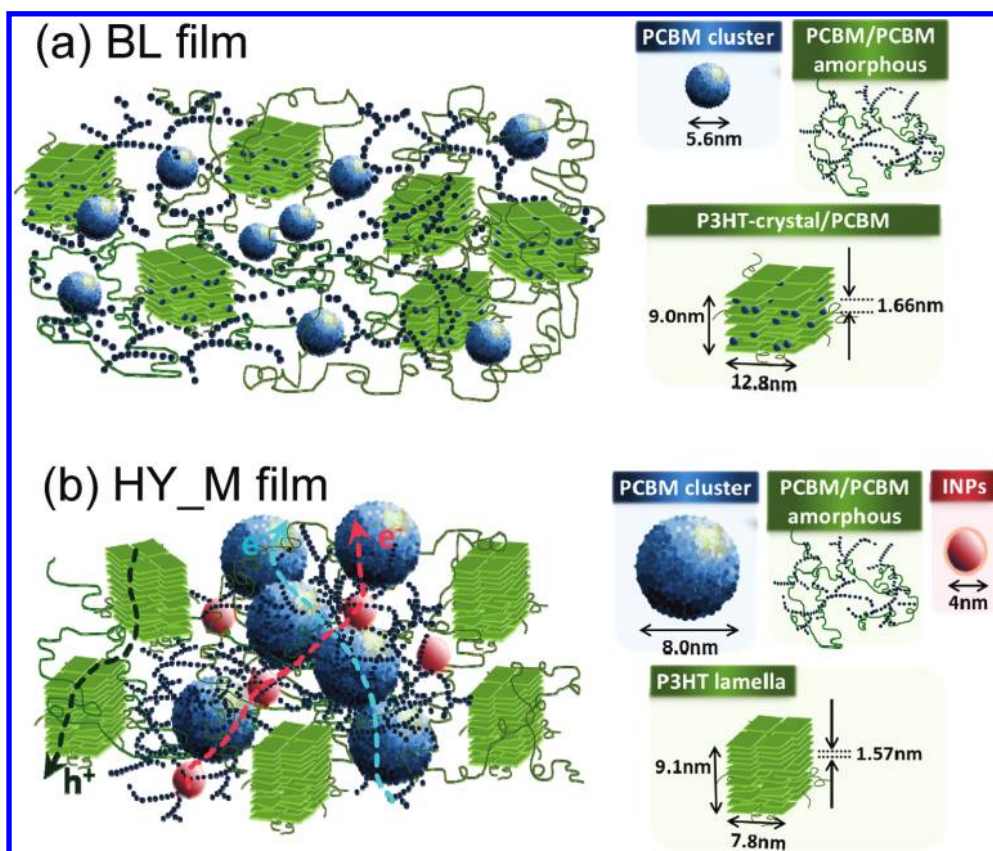


**Figure 4.** Schematic representation of the spatial arrangement of PCBM clusters, P3HT-crystal/PCBM domains, and the PCBM/P3HT amorphous domains in the phase-separated BHJ morphology of (a) P3HT/PCBM blended film (BL) and (b) P3HT/PCBM/Cu$_2$S INPs (HY_M) hybrid film. The nanoparticle-tuned nanostructure in (b) provides a much more effective transporting pathway through conventional interconnected PCBM clusters (light blue) or INP-containing network in the PCBM/P3HT amorphous domain coupled with interconnected PCBM clusters (light red).

The GISAXS analysis is listed in Table 1. The GISAXS analysis of the blended films with and without annealing (BL and BL_A films) demonstrates that the thermal effect significantly enhances the volume fraction (from 6.1 to 20%) and growth (from 2.8 to 4.9 nm in radius) of PCBM clusters. This result is consistent with the previous study.[7] However, the GISAXS analysis of the hybrid films suggests that the development of volume fraction of PCBM clusters due to the thermal annealing is largely depressed by the presence of INPs. In other words, the nanoparticle-tuned nanostructure remarkably limits the increasing volume fraction of the PCBM

cluster during thermal treatments. It may be attributed to the dispersion or network of Cu$_2$S INPs intercalated with polymer chains that can block the movement of thermal diffusion of PCBM molecules in the film. Therefore, the probability of forming PCBM clusters is largely reduced. In conclusion, this distinctive phase with a strong interaction among INPs, P3HT amorphous chain, and intercalated PCBM molecules confines the diffusion of PCBM in the phase and thus depresses the aggregation of PCBM clusters and is insensitive to thermal treatments. Moreover, this phase with high density of PCBM molecules intercalated with
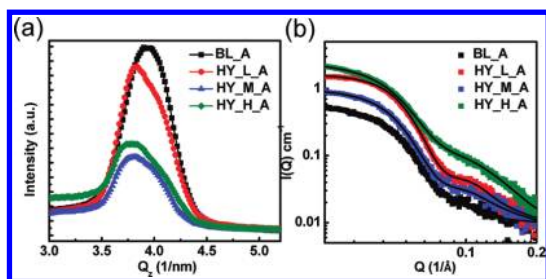
**Figure 5.** (a) GIWAXS and (b) GISAXS profiles of the annealed P3HT/PCBM blended film (BL_A), and P3HT/PCBM/Cu₂S INPs hybrid films (HY_L_A, HY_M_A, and HY_H_A). The solid lines represent the fitted GISAXS intensities.

P3HT amorphous chain and INPs has a special network-like zone for pathway of transporting charge carrier (Figure 4b). The finding potentially provides a rational approach to control the nanostructure of BHJ film for not only improving the device performance but also exhibiting excellent thermal stability.

**Hybrid Structure Property—Performance Correlation.** The device performance and the EQE curves of the annealed films are presented in Figure 6a,b, respectively. The photovoltaic characteristics as well as the electron mobility (obtained from space charge limited current (SCLC) measurement, see Supporting Information, Figure S7) are summarized in Table 1. Due to the improvement of interlayer contact between the active layer and the cathode Al during the postproduction annealing process, all of the summarized characteristics (open-circuit voltage ($V_{oc}$), short-circuit current density ($J_{sc}$), fill factor (FF), PCE, and electron mobility ($\mu_e$)) are largely enhanced compared to the as-casted case. According to the device performance, the short-circuit current density of the nanoparticle-tuned nanostructure is much higher than that of the regular blended solar cell, leading to the 23% of enhancement of PCE (from 3.5 to 4.3%), mostly contributed from the improved short-circuit current. For the EQE spectrum (Figure 6b), basically the EQE curves of the P3HT/PCBM/Cu₂S INP hybrid solar cell are better than that of P3HT/PCBM blended solar cell. The HY_M_A hybrid solar cell demonstrates the significantly improved EQE due to the nanoparticle-tuned nanostructure. The improved EQE suggests that, beside the conventional transporting route through PCBM clusters (light blue route in Figure 4b), the distinctive network with dense PCBM molecules formed by the dispersion of Cu₂S provides an alternative pathway of charge carriers transporting toward the electrode. The shape of EQE profiles can further provide supportive information of such a distinctive network. It is known that the EQE in the UV wavelength region is mainly contributed from the PCBM phases. The EQE profiles in Figure 6b exhibit photocurrent peaks shifted from 380 nm of the BL device to 350 nm of the P3HT/PCBM/Cu₂S INP hybrid devices. It suggests that the photocurrent in the UV region of the BL device is contributed from the
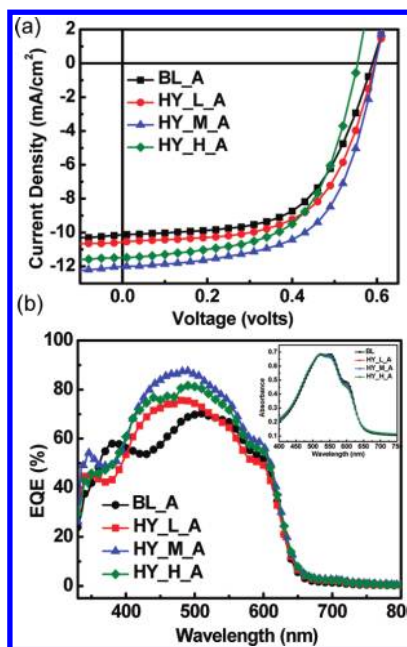


**Figure 6.** (a) $J$–$V$ curves and (b) EQE spectrum and absorption spectrum (inset) of the annealed devices with BHJ film of BL_A, HY_L_A, HY_L_A, and HY_L_A.

considerably large fraction of PCBM clusters (~20%) with optical absorption in longer wavelength (~380 nm). On the other hand, the photocurrent in the UV region of hybrid films is a result from the PCBM molecules which exhibit optical absorption in shorter wavelength (~350 nm) and provide large an amount of interface with P3HT phases. Consequently, once the PCBM molecules harvest sun light, the separated free carriers can effectively transport through the distinctive network in the PCBM/P3HT amorphous domain (as schemed in Figure 4b of the light red transport pathway), leading to the photocurrent peak at 350 nm. Furthermore, considering the improved EQE in the visible light region, while the separated free electrons from generated excitons in P3HT phases in the BL device can only transport through interconnected PCBM clusters, the free electrons in HY_M_A device have excellent transport routes within the nanoparticle-tuned nanostructure, through either the conventional interconnected PCBM clusters (light blue pathway in Figure 4b)[7,34] or the INP-containing network in the PCBM/P3HT amorphous domain coupled with interconnected PCBM clusters (light red pathway in Figure 4b). As a result, the electron mobility is enhanced from $1.6 \times 10^{-5}$ of BL film to $1.3 \times 10^{-4}$ cm²/(V·s) of HY_M_A film, which leads to the significantly improved device performance and EQE. It is noteworthy that, in addition to the proposed effects of improved carrier transport in the present work, the incorporated Cu₂S INPs also have other potentially positive effects on the photocurrent such as photoelectric conversion or optical scattering as proposed by Wang *et al.*[25] However, it can be observed that the EQE spectra of hybrid

films do not show any photocurrent contributed from wavelength longer than 650 nm. Hence, the photoelectric conversion effect of $Cu_2S$ INPs can be ruled out because the $Cu_2S$ INPs have lower band gap of 1.3 eV ($\sim$953 nm). Additionally, the inset of Figure 6b shows the absorption spectrum of BL_A, HY_L_A, HY_M_A, and HY_H_A films. Similarly, there is no observed optical absorbance from a wavelength longer than 650 nm even in the hybrid film with the highest incorporated amount (HY_H_A). Moreover, the spectra of films with incorporated $Cu_2S$ INPs do not present increased absorbance, thus the effect of optical scattering by the INPs can also be excluded. The exclusion of the two discussed effects (i.e., photoelectric conversion or optical scattering) can be attributed to the relative low concentration of INPs ($\sim 10^{-2}$ vol %) embedded in the hybrid films. Note that the less obvious absorption shoulders at 610 and 560 nm for hybrid films are a result from the less $\pi-\pi^*$ transition due to the slightly decreased crystallinity and interlayer and intralayer interaction (Figure 5a). In short, the proposed effect of enhanced electron transport in the hybrid film mainly attributes to the improved device performance.

For further investigating the effect of the amount of $Cu_2S$ INPs in the hybrid film on the device performance, we prepare the hybrid films with increased amounts of $6.2 \times 10^{-1}$, 2.4, 5.8, and 11.0 vol %. The corresponding $J-V$ curves and device performance of these hybrid films are shown in the Supporting Information, Figure S8 and Table 2, respectively. It is found that when the added amount is increased to 2.4 vol %, the corresponding PCE, short-circuit current density, and open-circuit voltage begin to dramatically drop (from 3.8 down to 1.9%) and finally reach 0.45% for the hybrid film with 11.0 vol % of $Cu_2S$ INPs. This result reveals that too large amount of $Cu_2S$ INPs would form the additional INP-rich (or aggregation-like) domain which does not contribute to the transportation pathway of the charge carrier and, instead, destructs the formation and distribution of PCBM clusters and even leads to local shunt and lowered open-circuit voltage. The results are consistent with the previous literature that the incorporating INPs destruct the transporting pathway for free carriers and thus significantly decrease the device performance.[28] Our work suggests that optimum amount of incorporated $Cu_2S$ INPs would lead to the nanoparticle-tuned nanostructure which can remarkably enhance the transporting behavior and device performance. There is a fundamentally interesting issue "whether other kinds of INPs are available to the proposed approach of nanoparticle-tuned nanostructure". For testing this

TABLE 3. Photovoltaic Device Characteristics of P3HT/PCBM blend (BL_A) and P3HT/PCBM/CdSe INP Hybrid Films with $1.2 \times 10^{-2}$ vol % (HY_L_A), $6.2 \times 10^{-2}$ vol % (HY_M_A), and $6.2 \times 10^{-1}$ vol % (HY_H_A) of CdSe INPs

| BHJ films | $V_{oc}$ (V) | $J_{sc}$ (mA/cm$^2$) | FF (%) | PCE (%) |
|---|---|---|---|---|
| BL_A | 0.59 | 10.1 | 59 | 3.5 |
| HY_L_A | 0.60 | 10.7 | 62 | 4.0 |
| HY_M_A | 0.60 | 11.1 | 63 | 4.2 |
| HY_H_A | 0.57 | 10.5 | 58 | 3.6 |

approach, we used CdSe with similar size ($\sim$4 nm; see Supporting Information, Figure S1) as INPs to prepare the P3HT/PCBM/CdSe INP hybrid film in a similar way. The $J-V$ curves (Supporting Information, Figure S9) and performance characteristics (Table 3) demonstrate the same characteristics and the improvement of performance (PCE improved from 3.5 to 4.2%) as a function of the amount of incorporated CdSe INPs. Therefore, it is demonstrated that INP-tuned P3HT/PCBM system is a promising strategy for good control of the BHJ morphology.

## CONCLUSIONS

We systematically study the phase-separated nanostructures of P3HT/PCBM/$Cu_2S$ INP hybrid solar cells with different amounts of INPs using simultaneous GISAXS and GIWAXS technique. The structural characteristics are well correlated to the device performance and photovoltaic properties. The nano-organized nanostructure of the active layer can be remarkably tuned by a certain amount of incorporated INPs. Without any current treatment, the specific INP-containing phase can assist the aggregation of PCBM molecules into the clusters during phase separation of film formation. Moreover, the distinctive nanoparticle-tuned nanostructure has the thermal stability during the thermal annealing. The network of the dispersed INPs forming an additional interpenetrating network provides a more efficient pathway for transport of charge carriers and thus significantly enhances the PCE value and photovoltaic properties. This result provides an important insight into the fundamental behavior and manipulation of phase separation in the active layer of the P3HT/PCBM-based system. The INP-tuned P3HT/PCBM BHJ solar cell presented for the first time can extend or combine with the current fabrication approaches. This approach is demonstrated to be an effective method that is beneficial to the design and fabrication of the highly efficient BHJ solar cells.

## EXPERIMENTAL METHOD

**Synthesis of INPs.** The details of $Cu_2S$ and CdSe INP synthesis can be found elsewhere.[37,38] The chemicals used were all of the purest quality available and used without further purification. In short, 1.25 mmol of ammonium diethyldithiocarbamate (Aldrich), 10 mL of dodecanethiol (Aldrich), and 17 mL of oleic

acid (Aldrich) were mixed in a 50 mL three-necked round flask. The solution was heated to 110 °C followed by injection of suspensions of 1 mmol copper acetylacetonate (Aldrich) dissolved in 3 mL of oleic acid. The reaction was then heated to 180 °C and kept for 15 min, allowing the growth and crystallization of $Cu_2S$ nanocrystals. Afterward, the solution was cooled to 120 °C

naturally followed by centrifuging under 4600 rpm for 10 min. Removal of the residual organic compounds was conducted by centrifuging the following typical solvent/nonsolvent procedure. The as-synthesized $Cu_2S$ INPs were hence capped with surface ligands oleic acid and can be well-dissolved in organic solvent. For the synthesis of CdSe INPs, briefly 0.041 g of CdO (Aldrich), 6.11 g of trioctylphosphine oxide (TOPO, Aldrich), and 3.05 g of hexadecilamine (HDA) were loaded in a 50 mL three-necked round flask and heated to 320 °C under Ar flow. Upon the color changed from brick red to transparent, the solution was cooled to 260 °C. A solution of 0.05 g of Se (Aldrich) in 2 mL of tri-$n$-butylphosphine (TBP) was swiftly injected into the flask. The CdSe INPs were allowed to grow at 260 °C for a minute and cooled by adding toluene. Similarly, typical solvent/nonsolvent clean procedure was conducted to remove the remaining TOPO and other organic compounds. The as-synthesized CdSe INPs well-dissolved in organic solvent were stabilized by surface ligand TOPO. It is noteworthy that, in the present study, $Cu_2S$ and CdSe INPs were used for synthesis without a further ligand exchange procedure. The transmission electron microscope (TEM) images of $Cu_2S$ and CdSe INPs are shown in the Supporting Information, Figure S1.

**Device Fabrication.** For the preparation of the P3HT/PCBM/INPs hybrid solution, 10 mg of regioregular P3HT ($M_w \sim 63\,000$, synthesized following the procedure demonstrated in ref 39) and 8 mg of PCBM (Nano-C, Inc.) were dissolved in 0.5 mL of chlorobenzene and stirred at 40 °C for 2 h. Subsequently, 0.5 mL of INPs ($Cu_2S$ or CdSe) dissolved in chlorobenzene with different concentration was added into the prepared P3HT/PCBM blended solution, leading to the obtained blended weight ratio (P3HT/PCBM/INPs) of 10:8:0.01, 10:8:0.05, and 10:8:0.5 respectively. The resulting concentrations of INPs are $5.6 \times 10^{-2}$, $2.8 \times 10^{-1}$, and 2.7 wt %, respectively. Therefore, considering the density of P3HT, PCBM, and $Cu_2S$ to be 1.1, 1.5, and 5.6 $g/cm^3$, respectively,[6] the theoretical volume fractions of the $Cu_2S$ INPs in HY_L, HY_M, and HY_H films are $1.2 \times 10^{-2}$, $6.2 \times 10^{-2}$, and $6.2 \times 10^{-1}$ vol %, respectively. Additionally, the control P3HT/PCBM binary blended solution was also prepared by mixing the P3HT (10 $mg\,mL^{-1}$) and PCBM (8 $mg\,mL^{-1}$) in chlorobenzene. For the layer-by-layer photovoltaic device fabrication, all of the solution-processed depositions were performed in air. Typically, transparent electrode ITO (Merck) was ultrasonically cleaned by a series of solvent (ammonia/$H_2O_2$/deionized water, methanol, isopropyl alcohol) before oxygen plasma treatment. A thin hole transport layer (40 nm) PEDOT/PSS (Baytron P 4083) was spin-coated on the substrate and then baked at 120 °C for 15 min. After cooling, the prepared active layer solutions were deposited by spin-coating at 700 rpm for a minute, leading to the film thickness of about 80 nm. The upper cathode Al ($\sim$100 nm) was thermally evaporated under high vacuum condition ($<2 \times 10^{-6}$ Torr), leading to the final device with an area of 0.06 $cm^2$. The devices with thermal treatments were preannealed (annealed before the cathode evaporation) at 90 °C for 15 min and postannealed (annealed with the cathode on the top) at 150 °C for 5 min. The fabricated photovoltaic devices were characterized using a solar simulator (Newport Inc., A.M. 1.5, 100 $mW/cm^2$) under air atmosphere. For the SCLC electron mobility measurement, the electron-only devices were fabricated by sandwiching the active layer between two Al electrodes. The current–voltage measurement of both SCLC and PCE was performed under air atmosphere using a Keithley 2400 source meter.

**Structural Characterization.** The GIWAXS and GISAXS measurements were conducted at the BL23 endstation of National Synchrotron Radiation Research Center (NSRRC), Taiwan. The thin films for characterization were deposited on a 2 cm × 1 cm silicon wafer. The details of instrumental setup can be found elsewhere.[8] In short, with the monochromated X-ray beam (8 keV, wavelength $\lambda$ = 1.55 Å, incidence angle = 0.25°), the GIWAXS and GISAXS signals were simultaneously collected by a CMOS flat panel X-ray detector (C9728DK, 52.8 mm square, situated 7.2 cm from the sample) and a CCD detector (MAR165, 165 mm in diameter, 1024 × 1024 pixel resolution, situated 287 cm from sample), respectively. On the basis of the setup, the

diffracted signal from P3HT lamellar crystallites can be covered from GIWAXS, and the effective $Q$ range of GISAXS ranged from 0.007 to 0.2 $Å^{-1}$. The 1D profiles were obtained by integrating the 2D patterns along $Q_X$ ($Q_X = 2\pi\lambda^{-1} \sin\vartheta \cos\alpha_f$) and along $Q_Z$ ($Q_Z = 2\pi\lambda^{-1}(\sin\alpha_i + \sin\alpha_f)$) for in-plane and out-of-plane directions, respectively.

*Conflict of Interest:* The authors declare no competing financial interest.

*Supporting Information Available:* TEM images of INPs $Cu_2S$ and CdSe. Two-dimensional pattern of GISAXS and GIWAXS of PO, BL, HY_L, HY_M, HY_H, BL_A, HY_L_A, HY_M_A, and HY_H_A films. GISAXS profiles including the $Q$ range ($<0.03$ $Å^{-1}$). Model fitting of GISAXS profile (BL_A) including the $Q$ range ($<0.03$ $Å^{-1}$). $J-V$ curves and mobility measurement (SCLC) of BL, HY_L, HY_M, and HY_H devices. Mobility measurement (SCLC) of BL_A, HY_L_A, HY_M_A, and HY_H_A devices. $J-V$ curves of P3HT/PCBM/$Cu_2S$ devices with largely increased amount of incorporated INPs. $J-V$ curves of P3HT/PCBM device (BL_A) and P3HT/PCBM/CdSe devices (BL_A, HY_L_A, HY_M_A, and HY_H_A). This material is available free of charge *via* the Internet at http://pubs.acs.org.

## REFERENCES AND NOTES

1. Li, G.; Shrotriya, V.; Huang, J.; Yao, Y.; Moriarty, T.; Emery, K.; Yang, Y. High-Efficiency Solution Processable Polymer Photovoltaic Cells by Self-Organization of Polymer Blends. *Nat. Mater.* **2005**, *4*, 864–868.

2. Ma, W.; Yang, C.; Gong, X.; Lee, K.; Heeger, A. J. Thermally Stable, Efficient Polymer Solar Cells with Nanoscale Control of the Interpenetrating Network Morphology. *Adv. Funct. Mater.* **2005**, *15*, 1617–1622.

3. Kim, Y.; Cook, S.; Tuladhar, S. M.; Choulis, S. A.; Nelson, J.; Durrant, J. R.; Bradley, D. D. C.; Giles, M.; Mcculloch, I.; Ha, C. S.; *et al.* A Strong Regioregularity Effect in Self-Organizing Conjugated Polymer Films and High-Efficiency Polythiophene:Fullerene Solar Cells. *Nat. Mater.* **2006**, *5*, 197–203.

4. Wu, J. L.; Chen, F. C.; Hsiao, Y. S.; Chien, F. C.; Chen, P.; Kuo, C. H.; Huang, M. H.; Hsu, C. S. Surface Plasmonic Effects of Metallic Nanoparticles on the Performance of Polymer Bulk Heterojunction Solar Cells. *ACS Nano* **2011**, *5*, 959–967.

5. Andersson, B. V.; Herland, A.; Masich, S.; Inganas, O. Imaging of the 3D Nanostructure of a Polymer Solar Cell by Electron Tomography. *Nano Lett.* **2009**, *9*, 853–855.

6. Bavel, S. S. V.; Sourty, E.; With, G. D.; Loos, J. Three-Dimensional Nanoscale Organization of Bulk Heterojunction Polymer Solar Cells. *Nano Lett.* **2009**, *9*, 507–513.

7. Liao, H. C.; Tsao, C. S.; Lin, T. H.; Chuang, C. M.; Chen, C. Y.; Jeng, U. S.; Su, C. H.; Chen, Y. F.; Su, W. F. Quantitative Nanoorganized Structural Evolution for a High Efficiency Bulk Heterojunction Polymer Solar Cell. *J. Am. Chem. Soc.* **2011**, *133*, 13064–13073.

8. Wu, W. R.; Jeng, U. S.; Su, C. J.; Wei, K. H.; Su, M. S.; Chiu, M. Y.; Chen, C. Y.; Su, W. B.; Su, C. H.; Su, A. C. Competition between Fullerene Aggregation and Poly(3-hexylthiophene) Crystallization upon Annealing of Bulk Heterojunction Solar Cells. *ACS Nano* **2011**, *5*, 6233–6243.

9. Chiu, M. Y.; Jeng, U. S.; Su, M. S.; Wei, K. H. Morphologies of Self-Organizing Regioregular Conjugated Polymer/Fullerene Aggregates in Thin Film Solar Cells. *Macromolecules* **2010**, *43*, 428–432.

10. Yu, B. Y.; Lin, W. C.; Wang, W. B.; Iida, S. I.; Chen, S. Z.; Liu, C. Y.; Kuo, C. H.; Lee, S. H.; Kao, W. L.; Yen, G. J.; *et al.* Effect of Fabrication Parameters on Three-Dimensional Nanostructures of Bulk Heterojunctions Imaged by High-Resolution Scanning ToF-SIMS. *ACS Nano* **2010**, *4*, 833–840.

11. Nguyen, L. H.; Hoppe, H.; Erb, T.; Gunes, S.; Gobsch, G.; Sariciftci, N. S. Effects of Annealing on the Nanomorphology and Performance of Poly(alkylthiophene):Fullerene Bulk-Heterojunction Solar Cells. *Adv. Funct. Mater.* **2007**, *17*, 1071–1078.

12. Li, G.; Yao, Y.; Yang, H.; Shrotriya, V.; Yang, G.; Yang, Y. "Solvent Annealing" Effect in Polymer Solar Cells Based on Poly(3-hexylthiophene) and Methanofullerenes. *Adv. Funct. Mater.* **2007**, *17*, 1636–1644.

13. Zhao, Y.; Guo, X.; Xie, Z.; Qu, Y.; Geng, Y.; Wang, L. Solvent Vapor-Induced Self Assembly and Its Influence on Optoelectronic Conversion of Poly(3-hexylthiophene):Methanofullerene Bulk Heterojunction Photovoltaic Cells. *J. Appl. Polym. Sci.* **2009**, *111*, 1799–1804.

14. Miller, S.; Fanchini, G.; Lin, Y. Y.; Li, C.; Chen, C. W.; Su, W. F.; Chhowalla, M. Investigation of Nanoscale Morphological Changes in Organic Photovoltaics during Solvent Vapor Annealing. *J. Mater. Chem.* **2008**, *18*, 306–312.

15. Bull, T. A.; Pingree, L. S. C.; Jenekhe, S. A.; Ginger, D. S.; Luscombe, C. K. The Role of Mesoscopic PCBM Crystallites in Solvent Vapor Annealed Copolymer Solar Cells. *ACS Nano* **2009**, *3*, 627–636.

16. Baek, W. H.; Seo, I.; Yoon, T. S.; Lee, H. H.; Yun, C. M.; Kim, Y. S. Hybrid Inverted Bulk Heterojunction Solar Cells with Nanoimprinted $TiO_2$ Nanopores. *Sol. Energy Mater. Sol. Cells* **2009**, *93*, 1587–1591.

17. Huang, J. S.; Chou, C. Y.; Liu, M. Y.; Tsai, K. H.; Lin, W. H.; Lin, C. F. Solution-Processed Vanadium Oxide as an Anode Interlayer for Inverted Polymer Solar Cells Hybridized with ZnO Nanorods. *Org. Electron.* **2009**, *10*, 1060–1065.

18. Kyaw, A. K. K.; Sun, X. W.; Jiang, C. Y.; Lo, G. Q.; Zhao, D. W.; Kwong, D. L. An Inverted Organic Solar Cell Employing a Sol—Gel Derived ZnO Electron Selective Layer and Thermal Evaporated $MoO_3$ Hole Selective Layer. *Appl. Phys. Lett.* **2008**, *93*, 221107.

19. Yu, H. K.; Dong, W. J.; Jung, G. H.; Lee, J. L. Three-Dimensional Nanobranched Indium Tin-Oxide Anode for Organic Solar Cells. *ACS Nano* **2011**, *5*, 8026–8032.

20. Wu, M. C.; Chang, C. H.; Lo, H. H.; Lin, Y. S.; Lin, Y. Y.; Yen, W. C.; Su, W. F.; Chen, Y. F.; Chen, C. W. Nanoscale Morphology and Performance of Molecular-Weight-Dependent Poly-(3-hexylthiophene)/$TiO_2$ Nanorod Hybrid Solar Cells. *J. Mater. Chem.* **2008**, *18*, 4097–4102.

21. Lin, Y. Y.; Chu, T. H.; Li, S. S.; Chuang, C. H.; Chang, C. H.; Su, W. F.; Chang, C. P.; Chu, M. W.; Chen, C. W. Interfacial Nanostructuring on the Performance of Polymer/$TiO_2$ Nanorod Bulk Heterojunction Solar Cells. *J. Am. Chem. Soc.* **2009**, *131*, 3644–3649.

22. Beek, W. J. E.; Wienk, M. M.; Janssen, R. A. J. Efficient Hybrid Solar Cells From Zinc Oxide Nanoparticles and a Conjugated Polymer. *Adv. Mater.* **2004**, *16*, 1009–1013.

23. Huyhh, W. U.; Dittmer, J. J.; Alivisatos, A. P. Hybrid Nanorod-Polymer Solar Cells. *Science* **2002**, *295*, 2425–2427.

24. Atwater, H. A.; Polman, A. Plasmonics for Improved Photovoltaic Devices. *Nat. Mater.* **2010**, *9*, 205–213.

25. Wang, D. H.; Kim, D. Y.; Choi, K. W.; Seo, J. H.; Im, S. H.; Park, J. H.; Park, O. O.; Heeger, A. J. Enhancement of Donor—Acceptor Polymer Bulk Heterojunction Solar Cell Power Conversion Efficiencies by Addition of Au Nanoparticles. *Angew. Chem., Int. Ed.* **2011**, *50*, 5519–5523.

26. Kim, K.; Carroll, D. L. Roles of Au and Ag Nanoparticles in Efficiency Enhancement of Poly(3-octylthiophene)/$C_{60}$ Bulk Heterojunction Photovoltaic Devices. *Appl. Phys. Lett.* **2005**, *87*, 203113.

27. Lee, J. Y.; Peumans, P. The Origin of Enhanced Optical Absorption in Solar Cells with Metal Nanoparticles Embedded in the Active Layer. *Opt. Express* **2010**, *18*, 10078–10087.

28. Topp, K.; Borchert, H.; Johnen, F.; Tunc, A. V.; Knipper, M.; Hauff, E. V.; Parisi, J.; Al-Shamery, K. Impact of the Incorporation of Au Nanoparticles into Polymer/Fullerene Solar Cells. *J. Phys. Chem. A* **2010**, *114*, 3981–3989.

29. Verploegen, E.; Mondal, R.; Bettinger, C. J.; Sok, S.; Toney, M. F.; Bao, Z. Effects of Thermal Annealing upon the Morphology of Polymer-Fullerene Blends. *Adv. Funct. Mater.* **2010**, *20*, 3519–3529.

30. Shin, M.; Kim, H.; Park, J.; Nam, S.; Heo, K.; Ree, M.; Ha, C. S.; Kim, Y. Abrupt Morphology Change upon Thermal Annealing in Poly(3-hexylthiophene)/Soluble Fullerene Blend Films for Polymer Solar Cells. *Adv. Funct. Mater.* **2010**, *20*, 748–754.

31. Cates, N. C.; Gysel, R.; Beiley, Z.; Miller, C. E.; Toney, M. F.; Heeney, M.; McCulloch, I.; McGehee, M. D. Tuning the Properties of Polymer Bulk Heterojunction Solar Cells by Adjusting Fullerene Size To Control Intercalation. *Nano Lett.* **2009**, *9*, 4153–4157.

32. Mayer, A. C.; Toney, M. F.; Scully, S. R.; Rivnay, S. J.; Brabec, C. J.; Scharber, M.; Koppe, M.; Heeney, M.; McCulloch, I.; McGehee, M. D. Bimolecular Crystals of Fullerenes in Conjugated Polymers and the Implications of Molecular Mixing for Solar Cells. *Adv. Funct. Mater.* **2009**, *19*, 1173–1179.

33. Huang, Y. C.; Tsao, C. S.; Chuang, C. M.; Lee, C. H.; Hsu, F. H.; Cha, H. C.; Chen, C. Y.; Lin, T. H.; Su, C. J.; Jeng, U.; *et al.* Characterization of Bulk Heterojunction Polymer Solar Cells with Different Fullerene Derivatives. *J. Phys. Chem. C*, submitted for publication.

34. Kiel, J. W.; Eberle, A. P. R; Mackay, M. E. Nanoparticle Agglomeration in Polymer-Based Solar Cells. *Phys. Rev. Lett.* **2010**, *105*, 168701.

35. Griffith, W. L.; Triolo, R.; Compere, A. L. Analytical Scattering Function of a Polydisperse Percus-Yevick Fluid with Schulz- (Γ-) Distributed Diameters. *Phys. Rev. A* **1987**, *35*, 2200–2206.

36. Kline, S. R. J. Reduction and Analysis of SANS and USANS Data Using IGOR Pro. *J. Appl. Crystallogr.* **2006**, *39*, 895–900.

37. Wu, Y.; Wadia, C.; Ma, W.; Sadtler, B.; Alivisatos, A. P. Synthesis and Photovoltaic Application of Copper(I) Sulfide Nanocrystals. *Nano Lett.* **2008**, *8*, 2551–2555.

38. Liu, I. S.; Lo, H. H.; Chien, C. T.; Lin, Y. Y.; Chen, C. W.; Chen, Y. F.; Su, W. F.; Liou, S. C. Enhancing Photoluminescence Quenching and Photoelectric Properties of CdSe Quantum Dots with Hole Accepting Ligands. *J. Mater. Chem.* **2008**, *18*, 675–682.

39. Wu, M. C.; Liao, H. C.; Chou, Y.; Hsu, C. P.; Yen, W. C.; Chuang, C. M.; Lin, Y. Y.; Chen, C. W.; Chen, Y. F.; Su, W. F. Manipulation of Nanoscale Phase Separation and Optical Properties of P3HT/PMMA Polymer Blends for Photoluminescent Electron Beam Resist. *J. Phys. Chem. B* **2010**, *114*, 10277–10284.